CORA Cork Open Research Archive
Cartlann Taighde Oscailte Chorcaí

Title	Sub-100 nm Feature Definition Optimization using Cold Cs Beam Exposed Self-Assembled Monolayers on Au
Authors	O'Dwyer, Colm
Publication date	2004-01-01
Original Citation	O'Dwyer, C. (2004) 'Sub-100 nm Feature Definition Optimization using Cold Cs Beam Exposed Self-Assembled Monolayers on Au', 206th Meeting of the Electrochemical Society: Nanoscale Devices, Materials, and Biological Systems: Fundamental and Applications. Hilton Hawaiian Village, Honolulu, Hawaii, 3-8 October. New Jersey: The Electrochemical Society, 13, pp. 411-430.
Type of publication	Conference item
Link to publisher's version	http://www.electrochem.org/dl/pv/published/2004/2004.htm
Rights	© The Electrochemical Society, Inc. 2004. All rights reserved. Except as provided under U.S. copyright law, this work may not be reproduced, resold, distributed, or modified without the express permission of The Electrochemical Society (ECS). The archival version of this work was published in O'Dwyer, C. (2004) 'Sub-100 nm Feature Definition Optimization using Cold Cs Beam Exposed Self-Assembled Monolayers on Au', 206th Meeting of the Electrochemical Society: Nanoscale Devices, Materials, and Biological Systems: Fundamental and Applications. Honolulu, Hawaii, 3-8 October. New Jersey: The Electrochemical Society, 13, pp. 411-430.
Download date	2026-11-03 12:31:22
Item downloaded from	https://hdl.handle.net/10468/1004



University College Cork, Ireland
Coláiste na hOllscoile Corcaigh

SUB-100 nm FEATURE DEFINITION OPTIMIZATION USING COLD Cs BEAM EXPOSED SELF-ASSEMBLED MONOLAYERS ON Au

C. O'Dwyer

Institut de Recherche sur les Systèmes Atomiques et Moléculaires Complexes,
Laboratoire Collisions, Agrégats et Réactivité, UMR CNRS 5589,
Université Paul Sabatier, 118 route de Narbonne,
31062 Toulouse Cedex 4, France

ABSTRACT

The results of a study into the dependency of SAM coverage, subsequent post-etch pattern definition and minimum feature size on the quality of the Au substrate used in both physical mask and optical mask atomic nanolithographic experiments are presented in this paper. In comparison, sputtered Au substrates yield much smoother surfaces and a higher density of {111} oriented grains than evaporated Au surfaces. Phase imaging with an atomic force microscope shows that the quality and percentage coverage of uniform alkanethiol monolayer adsorption was much greater for sputtered Au surfaces. Exposure of the monolayer with a laser-cooled Cs beam allowed determination of the minimum Cs dose (2 monolayers) to expose the SAM with lateral force microscopy. Suitable wet-etching, with etch rates of 2.2 nm min^{-1}, results in optimized pattern definition. Utilizing these optimizations, features as small as 50 nm were achieved using both a sub-100 nm physical mask and optical standing wave mask.

INTRODUCTION

Over the last ten years, considerable research efforts have been devoted to developing processes for nanoscale feature definition below the diffraction limit. The pioneering work performed by Timp et al.[1,2] and McClelland et al.[3] used a method for nanostructure fabrication based on a standing optical wave to focus neutral atoms. The method does not use a physical mask or resist, but relied on optical forces to focus direct deposition of atoms on permanent structures. Since the atomic de Broglie wavelength is of sub-nanometer order at conventional atomic beam temperatures, the structure size was not subject to matter wave diffraction limitations. McClelland deposited deposit lines of Cr as narrow as 38 nm full width at half maximum, spaced by 213 nm. These early studies stimulated several variants in the field of neutral atom nanolithography using light masks.[3-5] Many of the atoms that are easily manipulated with atom optics are either highly reactive or volatile, so that they are not suitable for the creation of durable, permanent structures using direct deposition; consequently, the development of patterned chemical resist methods that are sensitive to alkali and other neutral atoms is worthwhile exploring.

Resist-Based Atomic Nanolithography

Utilizing resists in neutral atom nanolithography provides both a high sensitivity to neutral atoms and a high resolution.[6] These resists can be categorized into two classes: self-assembled monolayers (SAMs) of organic molecules, and materials deposited onto a

surface from a background vapour.[7] Berggren and co-workers[8] have demonstrated the modification of the chemical properties of a thin film made from a self-assembled monolayer (SAM) of organic molecules on a surface. They used a beam of metastable argon atoms patterned by a material mask instead of a light mask as described above.

Lithography at nanometer scales (< 100 nm) requires resists thin enough that they give features with reasonable aspect ratios between the horizontal and vertical dimensions. The use of self-assembled monolayers (SAMs) as suitable resists has been the subject of much recent research because they provide an opportunity to modify the properties of solid surfaces, and as a consequence, they are projected to be technologically important.[9-14] Among the many SAM systems that have been investigated, those made by adsorbing alkanethiols on single-crystal gold surfaces have been more frequently studied because of their ease of preparation and excellent stability.[15] SAMs have particular advantages for the fabrication of nanometer scale features relative to polymeric resists for a number of reasons. The molecular diameter of the species in the SAM is small (< 1 nm) and the corresponding films formed are sufficiently thin that they minimize scattering of incident particles or atoms within the film.[7,16] However, one major disadvantage is the lack of knowledge surrounding the reactive mechanism of the SAM, when exposed to an atomic flux of Cs, for example. To generate useful contrast to chemical etchants between exposed and unexposed regions, a sufficient dose of atoms must be provided, but it must not over-expose to outlying regions. Furthermore, the structure formation is strongly affected by migration, agglomeration and local interaction of the atoms deposited on the surface. Although the explicit behavior of such properties has not yet been widely investigated, details of the atom-surface interaction certainly plays a crucial role in atomic nanolithography experiments.

Alkanethiol Self-Assembled Monolayers on Au

The principal ingredient for obtaining self-assembly is a relatively strong interfacial binding asymmetry of the molecular constituents. In the alkanethiol SAM case, this asymmetry is provided by the sulfur affinity for gold, and a comparably strong lateral interaction (4-8 kJ mol^{-1} per CH_2),[17] arising from the van der Waals forces between the alkyl chains that compose the backbone of each alkanethiol molecule. This lateral interaction can be controlled by changing the length of the hydrocarbon. While the lateral interactions are well characterized, the sulfur-gold interaction in the alkanethiol-gold SAMs has remained the subject of frequent debate.[18] This is especially true in neutral Cs atomic nanolithography experiments where alkanethiol SAMs are utilized as positive resists. The modification of the SAM, which is believed to stem from the chemical modification of the Au-S bond, allows replication of a lithographic material mask down to submicron dimensions. Such submicron dimensions are possible due to the high density molecular coverage ($\sim 4 \times 10^{14}$ cm^{-2}) which corresponds to an extremely small minimum molecular unit area of 2 nm^2.

The fact that alkanethiols can both physisorb through van der Waals interactions which can be changed by varying the chain length, and chemisorb through the sulfur bond, provides an excellent framework for studying their role in nanolithography. Site specific changes in their affinity to the gold surface can be probed by chemical force microscopy using chemically modified tips, and lateral force microscopy, that can measure adhesion forces of the molecules to the surface. These techniques highlight alterations in their chemical and physical state.

A better knowledge of headgroup/substrate interactions is essential for any progress in the understanding of the structure and growth kinetics of SAMs and of their role in neutral Cs atomic nanolithography. Recently, the features sizes of patterns written into SAMs through techniques such as scanning near field photolithography (SNP),[19,20] dip-pen nanolithography[21] and microcontact printing[22,23] have been shown to be limited by the morphology of the granular metal surface which has represented a resolution limit for metal substrate based lithography. This resolution issue was addressed by Love et al.[24] who reported that Pd substrates yielded better post-etch resolution than their Au counterparts when coated with alkanethiol monolayers for nanolithographic purposes. We have recently reported[25] that a resolution limit of ~20 nm is found when 1-nonanethiol SAMs are adsorbed on sputtered Au substrates. The results indicated that the quality of the Au surface is paramount in realizing a low defect-density molecular monolayer. However, we have shown that monolayer adsorption even on single {111} terminated single crystal Au grain is prone to defects.

In all previous cases, atomically flat, single crystal surfaces were employed. Furthermore, when thermally evaporated Au surfaces were used as substrates for SAMs, oxidation of the sulfur was observed.[26] The rate of oxidation was dependent on the surface morphology of the polycrystalline Au: surfaces with lower areal densities of grain boundaries showed little oxidation. Lee et al.[26] have also shown that the degree of polycrystallinity of Au has an effect on the oxidation and degradation of the SAM over time. They postulate that an increase in the degree of polycrystallinity translates into an increased density of domains in the SAM which in turn allows for a higher defect density. They don't however, quantify to what extent this degradation affects the coverage and uniformity of the SAM. However, the exact reason why the morphology of the metal surface affects SAM coverage and subsequent pattern definition has not yet been investigated.

In this paper, we present the results of a study into the dependency of SAM coverage, subsequent post-etch pattern definition and minimum feature size on the quality of the Au substrate used in both physical mask and optical mask atomic nanolithographic experiments. In particular, this paper poses and answers key questions regarding the reproducibility of sub-100 nm patterning of alkanethiol monolayers on Au substrates by wet-etching techniques. Such information is derived from studies of the quality of the monolayer coverage and optimization of the etching mechanism. In the first section we present a detailed study of the sputtered Au substrates. We then outline and discuss our findings on the structure, uniformity and substrate dependent factors affecting the coverage by the SAM layer, using lateral force microscopy (LFM) in the subsequent section. We then present detailed analysis of the dependency of 1-nonanethiol exposure on the Cs atom dose and analysis of the etch rate of Au covered with exposed SAM molecules, so as to maximize etch pattern definition. This section is followed by observations of the first sub-100 nm features patterned into 1-nonanethiol on sputtered Au substrates using both physical and optical lithographic masks.

EXPERIMENTAL

The Si(100) substrates were loaded, as received, into the sputtering chamber. A 4 nm thick Cr adhesion layer was sputtered for 6 s at 1000 W and subsequently a 30 nm thick Au layer was sputtered for 60 s at 300 W. Both were sputtered at a base pressure of 8×10^{-6} Pa. Substrates coated in this manner are hereafter designated Au:1. A 4 nm thick Cr layer and a 30 nm thick Au layer were also coated onto Si substrates by thermal evaporation under similar conditions. These substrates are designated Au:2. Prior to any

treatment, both type of Au surfaces were cleaned in ethanol and immersed in a 3:1 mixture of H_2SO_4:H_2O_2 at 398 K for 5 minutes to remove any organic contaminants. After rinsing with deionized water, the Au samples were immediately placed in a 10^{-3} mol dm^{-3} solution of 1-nonanethiol $CH_3(CH_3)_8SH$ (95%, Aldrich) in reagent grade ethanol and then incubated at room temperature for over 24 h. In the 24 h period, a self-assembled monolayer of thickness ~1 nm formed. After incubation, samples were rinsed with ethanol and examined microscopically. All samples were exposed to the Cs atomic beam flux, detailed below. Etching of exposed samples was carried out using a water-based etching solution composed of 1 mol dm^{-3} KOH, 0.1 mol dm^{-3} $K_2S_2O_3$, 0.01 mol dm^{-3} $K_3Fe(CN)_6$ and 0.001 mol dm^{-3} $K_4Fe(CN)_6$.

The crystallinity characterization was carried out by grazing incidence X-ray diffraction (GIXRD)[27] with a step width of 0.01^0, using a Philips PW-1710 diffractometer with a Cu anode (radiation Kα of λ = 1.54186 Å). X-ray rocking curves were performed on a Rigaku X-ray diffractometer with CuKα radiation and were acquired by fixing the 2θ angle to that of the Au{111} reflection. X-ray rocking curves were acquired of the substrate and Cr layer in order to obtain the physical rocking curve of the Au overlayer by subtraction and deconvolution of all spectra.

All atomic force microscopy (AFM) and scanning tunneling microscopy (STM) examinations were performed in ambient laboratory conditions (pressure and temperature). AFM and STM characterization was performed with a PicoSPM (Molecular Imaging, Inc.) and a Nano-R AFM (Pacific Nanotechnologies, Inc.). The STM tips were mechanically cut from 250 μm Pt/Ir (80:20) wire, electrochemically etched/polished and tested on highly ordered pyrolytic graphite (HOPG). Unless otherwise stated, the STM images were acquired at a bias voltage of +1.50 V in constant height mode. Images were acquired with high gap impedances to maximize the contribution from the alkanethiol monolayer,[28,29] and in particular, gap impedances of ~7-10 GΩ[30] were required to resolve individual atoms. Atomic resolution STM images of monoatomic steps in a Au{111} single crystal, evaporated on mica and flame annealed was conducted in order to calibrate the vertical height. Atomically resolved STM of the Au surface used in the experiments was also conducted to determine the crystallographic orientation of the sample with respect to the STM scan direction. Atomic resolution and topological AFM imaging was performed in both contact and AC tapping modes. Topological information was supplemented by lateral force and phase modulation imaging respectively to determine adhesion force changes and composition differences in the surfaces examined. Soft Si_3N_4 tipped cantilevers with a spring constant of 0.12 nN nm^{-1} were used in contact mode. Comparisons were made with STM images to examine whether any tip-induced reconstruction of the monolayer took place during imaging under STM.

Transversely Cooled Cs Atomic Beam

Figure 1 shows a schematic diagram of the collimated Cs beam. A thermal oven source heats a Cs metal reservoir to 373K. A Cs atomic beam effuses through an output nozzle, a long narrow tube 36 mm in length, 1.6 mm diameter. Optical molasses[31] cools the transverse velocity components of the beam, resulting in a 'bright' Cs atom beam[32], highly collimated to a divergence < 1 mrad along the *z* direction. The beam has a forward flux density of ~10^{12} atoms cm^{-2} s^{-1}.

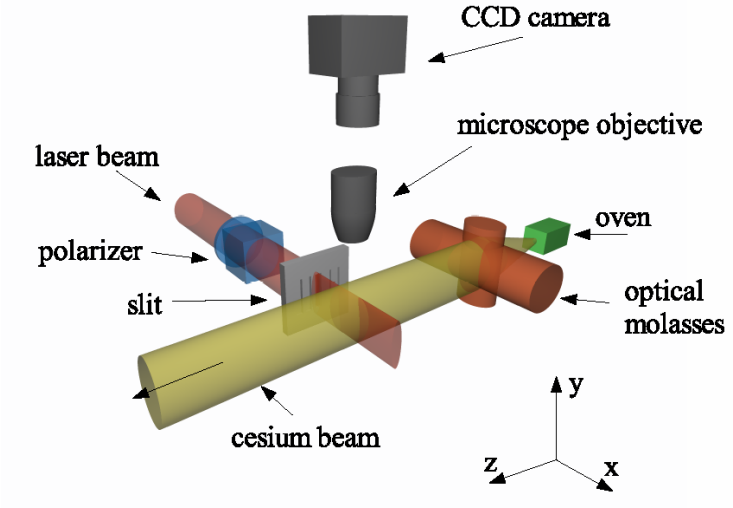


Figure 1. Atomic cesium beam effuses from a thermal oven and is collimated by transverse optical cooling to a divergence of less than 1 mrad with a forward flux density of 10^{12} cm^{-2} sec^{-1}.

RESULTS AND DISCUSSION

I. Comparison of Sputtered and Evaporated Au Surfaces

Non-contact tapping mode AFM was employed to characterize the topography of both the Au:1 and Au:2 surfaces.

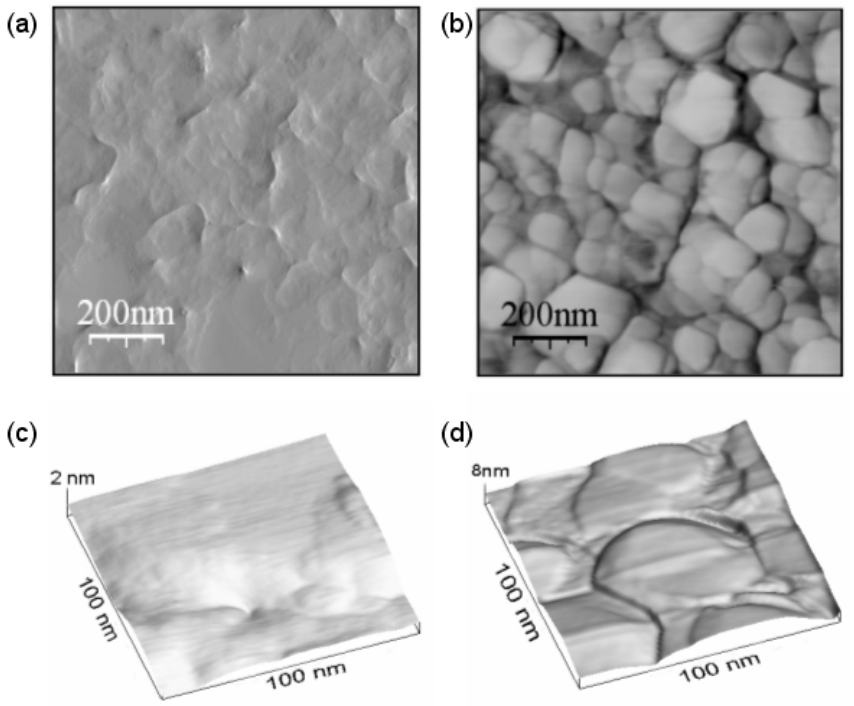


Figure 2. (a) 1 μm × 1 μm tapping mode AFM image of the sputtered Au:1 surface immediately prior to immersion in the alkanethiol solution. (b) 1 μm × 1 μm tapping mode image of the evaporated Au:2 surface identical imaging conditions. (c) 100 nm × 100 nm higher magnification image of the Au:1 surface showing a relatively smooth surface. (d) 100 nm × 100 nm higher magnification AFM image of the rougher Au:2 surface with multiple grains.

Figures 2a and 2b show the surface topography of the Au:1 and Au:2 surfaces respectively. It can be observed that the Au:2 surface is much rougher than that of the Au:1 surface and contains a well pronounced grain structure. The *rms* roughness of the Au:1 and Au:2 surfaces was determined from the AFM data in Figs. 2a and 2b and is measured to be 1.8 ± 0.4 nm and 6.7 ± 1.2 nm respectively. Such smooth Au:1 surfaces are formed by sputtering at low power, which was necessary to produce a smooth surface over a granular 4 nm thick Cr adhesion layer. This is highlighted more clearly in the magnified image of the surface in Fig. 2c. In Fig. 2d, which is a magnified AFM image of the highly granular Au:2 surface shown in Fig. 2b, the undulating grain structure is clearly observed.

High resolution AFM imaging of the Au:1 surface was also conducted to characterize the surface morphology and growth mechanism of the very smooth grains observed. This was not possible, however, for the highly undulating rough Au:2 surface. Figure 3a shows a 200 × 200 nm AFM image of the Au:1 surface in height-mapped grayscale. A line scan through the 'terraced' area of the surface, indicated on the image, is shown in Fig. 3b. It is observed that the height difference between each of the Au terrace layers is approximately 0.25 nm, almost equivalent to the Au monoatomic step height (0.2355 nm), indicating that Au monolayers (defined in the images by the terraces within the grain) are formed by 2D Stranski-Krastanov island/monolayer growth, are atomically flat and thus single crystal. Highlighted in the image are examples of individual monoatomic depressions of the Au surface. Such depressions are noted to be present over the whole surface and we have recently shown that these pits can increase the defect density of any organic monolayer adsorbed on the surface.[25]

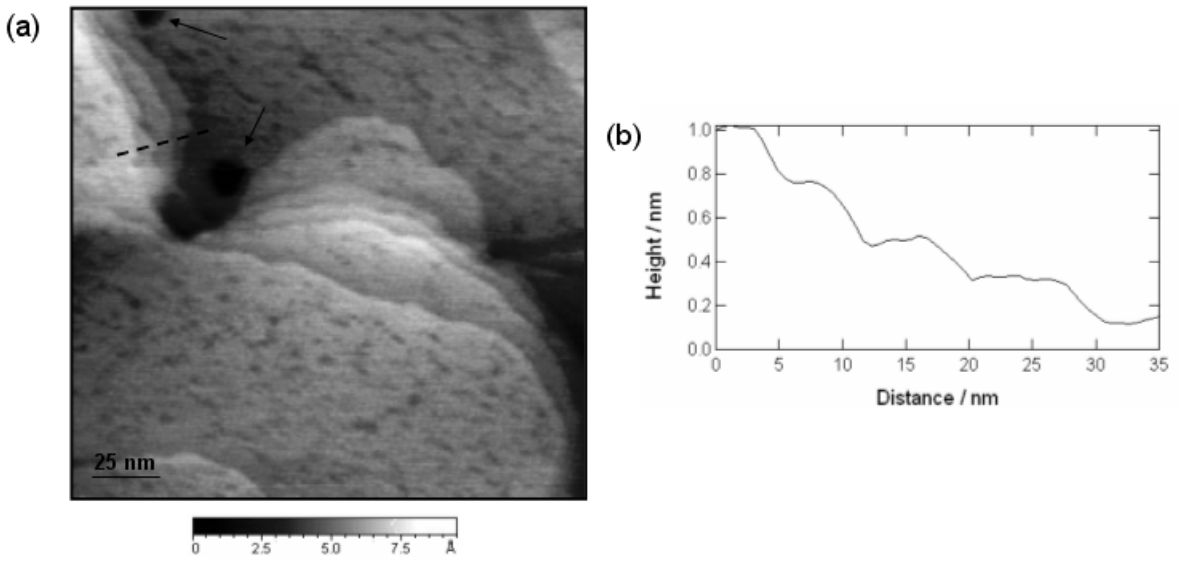


Figure 3. (a) 200 nm × 200 nm high resolution tapping mode AFM image of the Au:1 surface shown in height-mapped grayscale, featuring 0.25 nm high monoatomic terraces and grain boundaries. The terrace edges are delineated by the {111} planes of the Au lattice. Examples of monoatomic depressions in the Au surface are highlighted by arrows. (b) Height variation of successive monoatomic Au step edges on single crystal Au{111} showing the 0.24 nm step edges. This data represents the indicator line in the upper left of (a).

II. Determination of Grain Size, Density and Crystal Orientation

Constant current STM images were also acquired of various regions of both the Au:1 and Au:2 surfaces under ambient conditions in air to determine the average grain size. Images were obtained at sample bias between 50 and 200 mV and tunneling current between 1 and 2 nA. STM images of the Au:1 and Au:2 surfaces are shown in Fig. 4a and 4b, where individual grains are resolved. We employed fractal analysis to analyze the grain structure responsible for the surface roughness observed in the STM topographies and used a suitable autocorrelation function to determine the grain size. Such an approach allows us to correlate the measured fractal dimension of the STM measurements to a fractal dimension which characterizes the roughness of the surface.

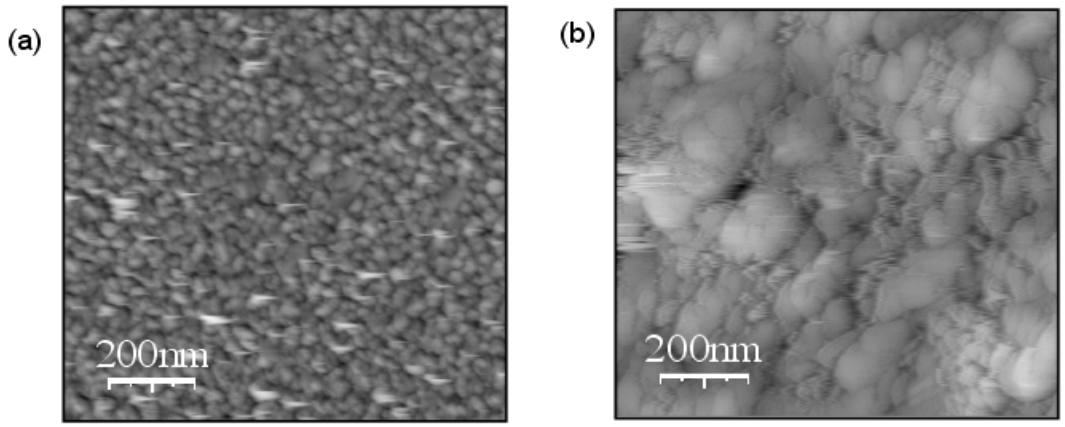


Figure 4. (a) 1 μm × 1 μm STM image of the Au:2 surface showing the high density of small grains. (b) 1 μm × 1 μm STM image of the smoother Au:1 surface showing a lower density of grains. Both images were acquired under constant current conditions at a bias of +2 V and a tunneling current of 1 nA.

The fractal dimension, D, of the film surfaces has been analyzed using a modified 'slit island' technique.[33] This method is based upon the perimeter-area relationship developed by Mandlebrot.[34,35] This relationship tells us that if an object with fractal dimension D is sliced, the perimeter and area of the resulting surface will fulfill the following relation:

$$(perimeter)^{\frac{1}{D-1}} \propto (area)^{\frac{1}{2}} \qquad (1)$$

where D-1 is the fractal dimension of the slice. Different slices of the same object follow the same relation. Thus, in a graph of *log*(perimeter) versus *log*(area) for different slices, the slope of the corresponding line will be (D-1)/2.[34,35] In the present case, the STM images are 'sliced' by creating contour maps to which we apply a fractal analysis.[33-35] The obtained fractal dimensions determined from the STM images give values of 2.02 and 2.26 for the Au:1 and Au:2 surfaces respectively. The overall surface topography of the Au:1 surface is relatively homogeneous, whereas for Au:2 surfaces, the grain structures responsible for the roughness are clearly visible. The obtained fractal dimension characterizes the influences of the granular structure on the roughness of the respective surface.[33] For sputtered Au substrates, the value of D reduces and the fractal dimension approaches the value 2, indicating a smooth 2-dimensional surface.[33] The grain structures align themselves parallel to the substrate orientation to produce a smoother surface.

From the STM topographies, an estimation of the grain size has been carried out using the autocorrelation function approach.[36] The autocorrelation function, defined as:

$$acf(a) = \int i(\mathbf{a})i(\mathbf{a}+\mathbf{r})d\mathbf{r} \qquad (2)$$

where $i(\mathbf{r})$ is the signal intensity or measured tunneling current of a given ATM scan and $i(\mathbf{r} + \mathbf{a})$ is the signal intensity $i(\mathbf{r})$ measured at a characteristic distance $|\mathbf{a}| = 1/N$, where N is the number of points in a particular scan. The net effect of such computation would be strong peak-like features that correspond to correlated regions of the surface being scanned. The separation distance between these peaks would then replicate the average grain size distribution.[33] This procedure is repeated for each image of the same sample and the results are averaged. The average grain sizes determined in this way from the STM data in Figs. 4a and 4b give values of 150 nm and 45 nm for the Au:1 and Au:2 surfaces respectively. Thus the larger grain size observed on the smoother Au:1 surface is advantageous for the adsorption of a relatively uniform nonanethiol monolayer, whereas the highly rough undulating granular surface morphology of the Au:2 substrates present a much more varied surface topography, unfavorable for controlled alkanethiol adsorption.

It is well understood that alkanethiol adsorption is dependent on the crystal orientation of the Au grains and the SAM monolayer uniformity is dependent on the density of grains with the same crystal orientation. We have employed GIXRD to characterize the crystal orientation of the grains in both the Au:1 and Au:2 surfaces and to quantify the relative density of each crystal orientation in both surfaces. The GIXRD spectra of the Au layers' crystal structure is shown in Fig. 5a. For the Au:1 layer, two peaks were observed in the spectrum at 38.15^0 and 88.3^0, which correspond to the {111} and {222} planes of the face-centered cubic structure of bulk Au, respectively. For the Au:2 layer, however, a number of peaks were observed at 38.15^0, 44.35^0, 64.6^0, 77.9^0 and 83.8^0, corresponding to the {111}, {200}, {220}, {311} and {222} planes. The inter-planar spacing of the sputtered Au layer, determined from the diffraction angle of the {111} plane in Fig. 5a, is measured to be 0.238 nm, in good agreement with that of the inter-planar spacing of bulk Au{111} (0.24 nm). In both cases, the {111} peak shows the highest relative intensity indicating that a greater density of these grains exist in both types of surfaces. However, for the Au:1 surface only two crystal orientations are observed and the difference in relative intensity between these two peaks indicates that the surface is almost entirely composed of {111} oriented Au grains. In contrast Au:2 contains a number of crystal orientations; even though the energetically favorable {111} grain density is highest, as can be seen from Fig. 5a, this density is just a fraction of that for the Au:1 surface.

In Fig. 5b, the normalized {111} reflections for both the Au:1 and Au:2 surfaces are overlayed. Individual fitting of the diffraction peaks was carried out using the Philips APD program that fits the sample-dependent variables (angle position, intensity and line broadening) to the experimental diffraction profile using a Marquardt nonlinear least-squares algorithm. It is observed that the Au:1 exhibits a higher relative intensity than the Au:2 surface by a factor of ~1.5. Furthermore, the {111} Bragg reflection from the Au:1 surface has a narrower linewidth, indicating the degree of crystallinity in the Au:1 is greater than that of the Au:2 surface. This implies that the grains sizes for the Au:1 surface are greater than those on the Au:2 surface, which is in good agreement with the STM information. From Fig. 5, the quantitative percentage of {111} terminated surface on Au:1 and Au:2 can be determined. A value of 0.94 is estimated for the fraction of the surface terminated with this crystal orientation. For the Au:2 surface, however, the presence of grains with different crystal orientations automatically implies that the

percentage of surface terminated by the Au{111} face is less than that for the Au:1 surface. The fraction of the surface terminated with the {111} face for the Au:2 is estimated to be 0.49, almost half that for the Au:1 surface, which agrees well with the high resolution {111} GIXRD curves in Fig. 5b.

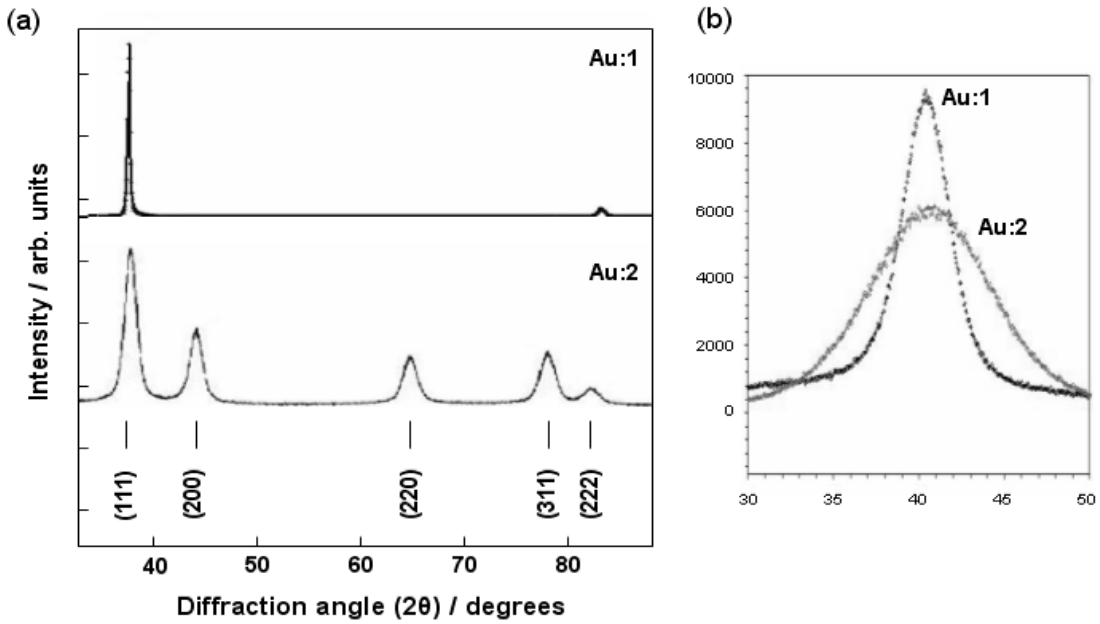


Figure 5. (a) GIXRD spectra of the Au:1 and Au:2 layers. The spectra were acquired at grazing incidence to determine the preferential orientation of the grains without substrate contributions. On a logarithmic scale, no discernable peaks from {200}, {220} or {311} reflections of the Au lattice could be observed for the Au:1 surface. (b) High resolution normalized GIXRD spectra of the Au:1 and Au:2 layers for the {111} peak overlaid for comparison. The units are the same as those for (a).

Thus, AFM, STM and GIXRD studies of the sputtered (Au:1) and evaporated (Au:2) surfaces used, shows that sputtered Au surfaces exhibit a much lower degree of roughness. Furthermore, sputtered Au surfaces contain a higher density of {111} oriented Au grains, a distinct advantage for the adsorption of alkanethiols.[25,30] Evaporated Au surfaces however, are not only rougher, but contain grains of multiple crystal orientations. The average grains sizes for sputtered and evaporated Au surfaces are given in Table I. An important finding is that the majority of grains on Au:1 surfaces have the same crystal orientation, {111}.

This equiorientation of grains is beneficial for uniformity of alkanethiol coverage.[25] The smoothness of the SAM layer compared to the evaporated Au:2 layers, is due to the method of growth. As mentioned previously, the sputtered Au growth mechanism is 2D progressive island/monolayer growth. Furthermore, the 150 nm grain size perpendicular to the film is much greater than the SAM film thickness, suggesting that a pillar-like growth (which results for film thickness to grain size aspect ratios close to unity) formation does not occur for Au:1 films. The preferential growth of grains with the same crystal orientation to sizes ~3 times their thickness is close to single crystal epitaxial growth. The sole differences are the relative orientation of grains with the same crystal internal orientation and whether the grains are parallel to the surface or not. These deviations result in the measured roughness. Some monoatomic depressions exist on the

surface of each grain prior to treatment in the alkanethiol solution, but we have recently demonstrated that the alkanethiol covers the surface and depressions alike.[25,30] Thus sputtered Au films produce good quality substrates for alkanethiol based resist adsorption for sub-100 nm atomic nanolithography applications.

Alkanethiol Coverage and Dependence on Au Morphology

There have been numerous reports of substrate-induced effects on the quality of the patterns produced after etching in atomic nanolithography processes.[24,26] However, all such reports have apportioned blame for poor quality on either the roughness of the substrate or on the grain size. While these parameters certainly do have an effect on the coverage by alkanethiols of Au surfaces, thus far no analysis of alkanethiol coverage of Au substrate *prior* to the etching step have been performed. We have employed both phase imaging non-contact AFM and lateral force contact AFM techniques to characterize the SAM/Au surface immediately prior to use in nanolithographic experiments. Although grain size and surface roughness contribute, our studies have revealed that the coverage uniformity depends first and foremost on the crystal orientation of the grains.

As outlined in the previous section, sputtered substrates give smoother surfaces than evaporated Au surfaces and show a much lower density of grains. More importantly, however, the Au:1 surface also contains a much greater proportionate density of {111} oriented Au grains. The fraction of the surface displaying the crystal faces corresponding to these reflections is important because at least one of them, the {100} face, is associated with a noncommensurate arrangement of the monolayer lattice and correspondingly weaker SAM-Au bonding. There have been no reports of SAM adsorption on Au{200}, Au{311} or on Au{222}. Figures 6a and 6b show non-contact AFM images of the Au:1 and Au:2 surfaces respectively, with corresponding phase imaging. Both topographical and phase imaging were acquired simultaneously. Phase imaging allows the determination of the variation in composition of a particular surface. In this case, the alkanethiol monolayer is shown in black and the Au surface is white/bright gray. The AFM cantilever is vibrated to measure the force between a probe and surface during an AFM scan. Changes in the vibration amplitude or phase are easily measured and the changes can be related to the force on the surface. Thus the magnitude of amplitude damping and the amount of phase change of the cantilever depends on the surface chemical composition and the physical properties of the surface.

From Fig. 6, it can be observed that the percentage coverage of the Au:1 surface by the alkanethiol (black) is greater than that for the Au:2 surface. By numerical integration of monotone images such as the phase images in Figs. 6a and 6b, the percentage total coverage of the SAM was found to be 59% and 21% for Au:1 and Au:2 surfaces respectively. Interestingly, the percentage coverage of the Au:1 surface by the SAM is less than the percentage of coverage by {111} terminated Au faces. Such quantitative analysis gives valuable information on what influences the degree of uniformity in alkanethiol monolayers on Au. Firstly, the surface must have minimal roughness, a prerequisite for maximum coverage. Secondly, the degree of uniformity in the monolayer is increased, but not maximized, if the Au surface is composed of grains with a single crystal orientation. But most importantly, the GIXRD and AFM information implies that the substrate does not have to consist entirely of grains with the {111} crystal orientation if complete alkanethiol adsorption is to be realized, *i.e.* alkanethiol adsorption to other crystal orientations is possible. Any non-uniformities observed would

be due, then, to the presence of grain boundaries and other defects in both the Au surface and the adsorbed alkanethiol monolayer, as we recently reported.[25]

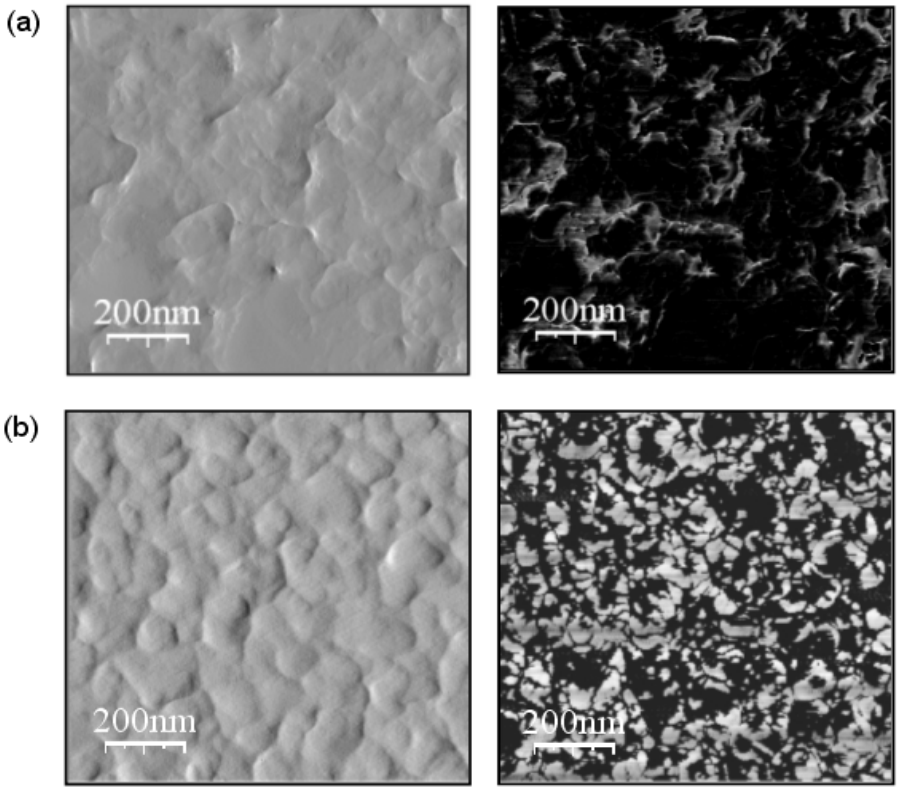


Figure 6. (a) Tapping mode AFM image of the alkanethiol monolayer covered Au:1 surface, and its corresponding phase image. (b) Tapping mode AFM image and corresponding phase image for the Au:2 surface covered with the alkanethiol monolayer. Imaging of both samples was done under identical conditions (laboratory and AFM parameters).

Atomically flat surfaces such as those found on Au:1 surfaces are conducive to the growth of ordered SAMs. Figure 7a shows an STM image of the alkanethiol SAM on the sputtered Au surface. Such large scale STM surface survey images show the highly variable coverage of the Au by the SAM on Au monoatomic terraces. The surface is observed to consist of a mosaic-like network of domains ranging in size from approximately 5-25 nm, with some defect-free domains observed to extend to more than 50 nm. It can also been observed that monolayer domains, highlighted in the image, are present over the full surface area of each terrace. More detailed analysis on the domain formation and characteristics can be found elsewhere.[25] Suffice it to say that the quality of the Au surface plays a critical role in determining the coverage quality by the monolayer. A higher magnification STM image of the monolayer on Au:1 is shown in Fig. 7b. It can be observed that each domain consists of an ordered arrangement of alkanethiol molecules. Indeed, the packing arrangement is identical and coherent within a single domain, *i.e.* all atoms are arranged such that the unit cell axes of the packing arrangement remain unchanged within the domain itself. Each of the domains are separated by domain boundaries that are typically of molecular scale dimensions. Such boundaries are identified in Fig. 6b as dark fissures between domains. Most boundaries are observed to have three orientations originating from the hexagonal Au{111} three-fold surface symmetry. These observations were all made on Au{111} single crystal

grains. Even with exceptionally ordered sputtered Au surfaces composed of predominantly {111} terminated Au planes, the relative orientation of each Au{111} grain with respect to another also adds to the density of features that make the molecular coverage non-uniform. Such boundaries are indicative of significant non-uniformity on the nanometer scale, implying limitations[25] on the resolution of patterning achievable when SAMs are employed as positive resists in atomic nanolithography experiments.

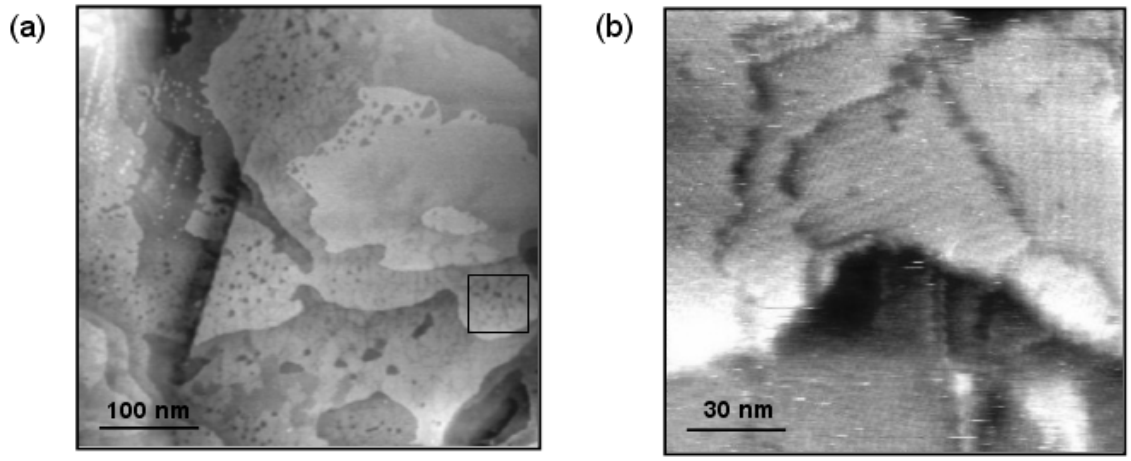


Figure 7. (a) 500 nm × 500 nm STM image of the 1-nonanethiol on Au{111} terraces, where a large number of non-uniformities such as domain boundaries, pinholes and monoatomic depressions are observed. A number of domains are highlighted in the image. (b) Higher resolution 30 nm × 30 nm STM image showing molecular scale domain boundaries and ordered alkanethiol molecule arrangement on Au{111} terraces.

III. Cs Exposure of Alkanethiol Monolayer and Optimization of Feature Resolution

Having characterized the influence of the Au surface on the coverage uniformity by the monolayer, we now turn to the exposure of this monolayer by a cold atomic Cs beam. Many groups report that alkanethiol resist based nanolithography is not very reproducible.[24,32] This lack of reproducibility is partially due to the quality of the Au substrate. However, for a complete lithographic process, the exposure of the alkanethiol with Cs atoms and the subsequent wet-etching steps are also critical stages in the eventual realization of the desired lithographic pattern. Various reports differ regarding the method of exposure of the alkanethiol molecules, the minimum Cs dose per molecule required to effect this exposure, the rate and anisotropy of the Au etching in suitable solutions. We have conducted detailed studies on all these issues to clarify the dependencies of all aspects of the nanolithographic process and the results are presented in this section.

With an atomic beam of Cs, transversely collimated and cooled by optical molasses, we have exposed the alkanethiol resists through a material mask consisting of a woven wire mesh (wire 30 μm diameter, 80 μm period). This relatively large periodic grid is easily imaged and thus amenable to systematic study. The alkanethiol coverage Au:1 substrate was exposed to the Cs beam for periods ranging from 5-30 mins at a flux density of ~10^{12} atoms cm^{-2} s^{-1}. After exposure the samples were immediately examined by AFM. Each AFM image was supplemented by lateral force microscopy (LFM) images of the surface taken simultaneously. LFM measures lateral deflections (twisting) of the cantilever that arise from forces on the cantilever parallel to the plane of the sample

surface and thus is sensitive to the detection of differences in adhesion properties of the monolayer. Figures 8a and 8b show an AFM and corresponding LFM image of the alkanethiol covered Au:1 substrates exposed to the Cs beam for 15 mins.

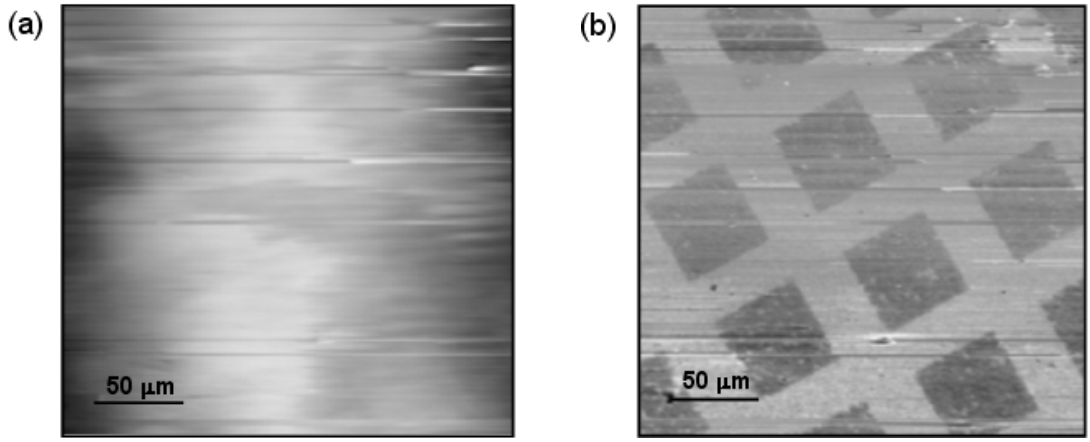


Figure 8. (a) AFM image of the alkanethiol covered Au:1 surface after 15 mins exposure to the Cs beam showing a featureless topography. (b) LFM image of the same surface acquired simultaneously showing the replicated mask pattern caused by changes in the adhesion of the monolayer to the Au surface by exposure to the Cs beam.

It is observed that the topography measured by the AFM is that of a smooth surface, with no grid-like features identical to the physical mask used in the exposure. In the adjoining LFM image, however, it can be clearly seen that the contrast shows a replica of the pattern, indicating that after 15 mins, the SAMs are sufficiently altered to be detected by LFM. These studies were also performed on samples exposed for 10 and 5 mins, but no features were observed with LFM in either case. Thus, the difference between exposed (but not etched) and unexposed SAMs on Au observed in the lateral force images is that the contrasting areas of the image, are due to contrasting tip-surface interaction forces. The darker contrasting areas represent the Cs-exposed SAM and indicating that the torsional force experienced by the cantilever in contact with the exposed SAM is relatively less than that due to unexposed SAM. This implies that the exposed SAM has a lower coefficient of friction due to adhesion to the polar surface of the Si_3N_4 tip employed in the imaging. Hence LFM is able to highlight and resolve the exposed pattern while there is no observable contrast in the topography.

In order to determine the minimum Cs dose, *i.e.* the number of Cs atoms required to render the SAM molecule susceptible to etching, the density of SAM molecules on the surface of the Au has first to be determined. This measurement was acquired from high magnification and high resolution AFM images, such as that shown in Fig. 9, which is an atomic resolution AFM image of the alkanethiol covered Au:1 surface. From these high resolution AFM images, the hexagonal $(\sqrt{3} \times \sqrt{3})R30^0$ molecular arrangement[25,30] can clearly be observed. An estimate for the density is ~4 molecules nm^{-2}. This value is in agreement with previous reports[37-39] and gives an estimate for the molecular occupational density of $\sim 4 \times 10^{14}$ cm^{-2}, assuming perfect hexagonal arrangement and no defects. Defects that appear as etch pits within the SAM monolayer can be ignored.[25,30] Only the domain boundaries can affect the density calculation but a typical domain boundary is of the order of 2-4 lattice spacings.

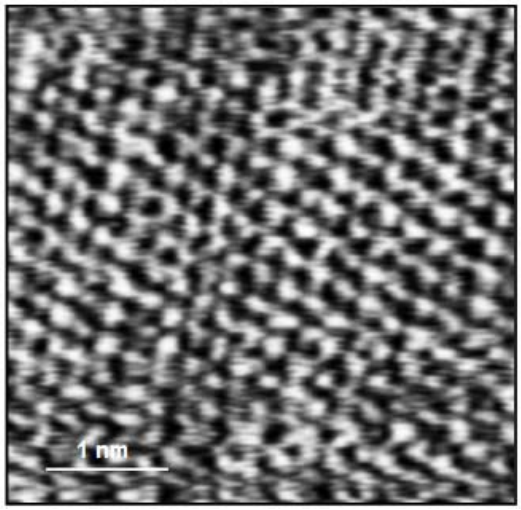


Figure 9. Non-contact AFM image with molecular resolution of the alkanethiol covered Au:1 surface, showing the hexagonal packing arrangement of the molecular monolayer. The nearest-neighbor molecules are commensurate with the Au{111} lattice along the [112] directions.

Thus, employing a Cs atomic beam with a flux of 10^{12} atoms cm^{-2} s^{-1}, 0.0025 atoms s^{-1} impinge on the surface per SAM molecule, with respect to the density of SAM on the Au surface. This flux implies a deposition rate of 0.15 monolayers min^{-1}. In order to determine the minimum number of Cs atoms needed to expose a SAM monolayer, the Au/SAM surface was exposed to the Cs beam for exposure times of 15 and 30 mins and then etched fully to remove all the underlying gold. Thus any gold not removed, but within the beam cross-section did not receive a sufficient exposure dose of Cs and this is quantifiable using the characteristics of both the Cs beam and the physical mask. Using the woven wire mesh mentioned previously, two samples were exposed and AFM images (post-etch) were acquired to determine the number of exposed square patterns either side of the position of the beam intensity maximum. This allows us to determine the dose that each part of the sample surface received. The feature dimensions were acquired from AFM images of the same surface so that the number of squares etched could be counted and converted to a real distance. Once acquired, this distance measurement was compared to the beam intensity profile, shown in Fig. 10, and converted to a corresponding intensity; thus the corresponding Cs dose could be estimated. The minimum Cs density is estimated to be approximately 7.5×10^{14} atoms cm^{-2}, which represents a minimum of ~2 Cs atoms per SAM molecule. Therefore ~2 monolayers of Cs are required to sufficiently alter the monolayer to render it susceptible to wet etching. This dosage translates into a minimum exposition time of ~13 mins and is in good agreement with the LFM studies of the Cs exposed alkanethiol monolayer discussed earlier in this section.

Thus, having determined the Cs dose necessary to expose an alkanethiol monolayer resist, optimization of the etching process is necessary to realize nano-scale lithographic patterns. The etching process requires a detailed study of the chemistry of the etching mechanism and etching nucleation processes of Au in ferricyanide-containing, water-based solutions. When clean gold is exposed to an aqueous solution of cyanide ions in the presence of a mild oxidant, which in this case is the ferro/ferricyanide complex, the gold dissolves.[40,41]

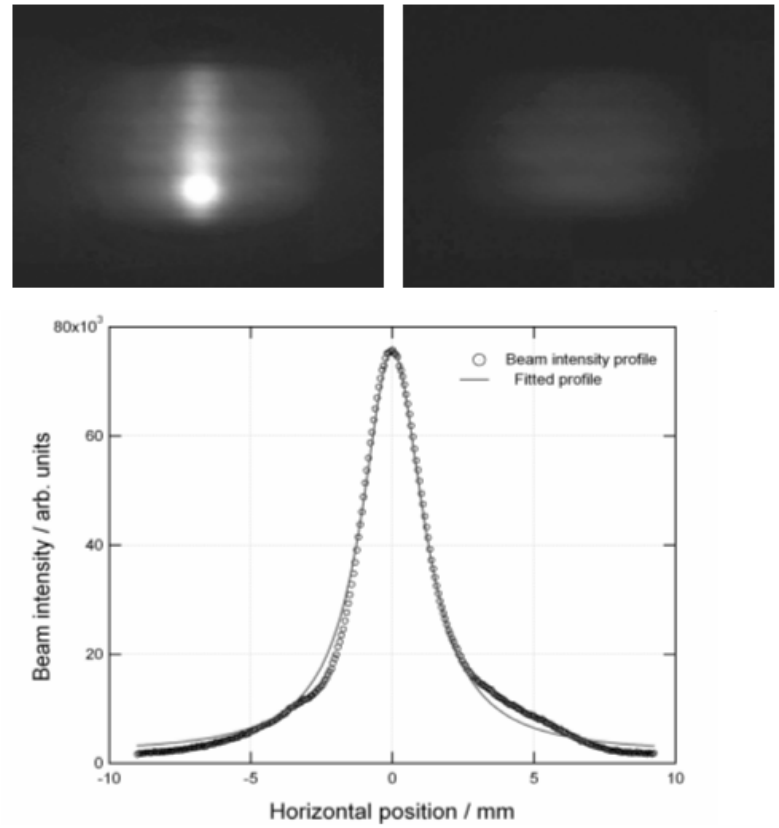


Figure 10. Cross-sectional image of the 2D collimated Cs atomic beam used during exposure of the alkanethiol monolayer and the corresponding cross-sectional beam intensity profile. This profile was acquired by a CCD camera.

The free energy of this process is dominated by the formation of the very stable and soluble $Au(CN)^{2-}$ ion according to:

$$Au + 2CN^- + Fe(CN)_6^{3-} \rightarrow Fe(CN)_6^{4-} + Au(CN)^{2-} \qquad (3)$$

All of the etching experiments were conducted using SAMs formed from 1-nonanethiol, $HS(CH_2)_8CH_3$, although it has been reported that alkanethiols having longer chains provide comparable protection against etching. Shorter chain alkanethiols provide some degree of protection, but their ability to resist etching decreases with the length of the chain. For a cyanide based etchant, the absorption of CN^- ions on metals, in particular Au, can decrease their oxidation potentials by up to 2 V.[42,43] Furthermore, the oxidation potential of Au can also be reduced by the chemisorption of sulfur-based compounds such as alkanethiols, but the magnitude of this reduction is much less than that for the CN^- ion.[42,43] Adsorption of CN^- to the Au surface is prevented if the Au surface is covered with an alkanethiol molecule such as 1-nonanethiol used in this work. Thus the protected regions dissolve at a much slower rate than the exposed areas.

For etching solutions based on the cyanide ion, there are two principal properties necessary for an effective, selective etching solution. The solution must not contain a coordinating ion that can disrupt, damage or remove the adsorbed alkanethiol monolayer, and it should contribute toward the reduction in the oxidation potential of the Au by adsorption to the surface. This solution must also include an oxidant that oxidizes the Au in the presence of the coordinating ion with relative ease and have little or no effect on

the alkanethiol monolayer. Thus the SAM must be impermeable and the oxidation of the Au must occur, most probably due to the redox potential of the oxidant being much lower than that of the Au. Ferricyanide, is such an oxidant. The necessary step involving the reduction of the oxidation potential of the Au is maintained by using ferricyanide in a thiosulphate solution. Thiosulphate has an effect similar to cyanide in that it can reduce this oxidation potential, although the decrease is not as large as observed with CN^- ions. In the electrolyte, used in this work, the ferricyanide oxidant, at a high concentration of 0.01 mol dm^{-3}, etches selectively comparable to CN^- based etchants.[43]

Numerous Au:1 samples were etched for various lengths of time in order to determine the actual etch rate. Each etching process was carried out under identical conditions and the resulting variation in height between the etched and unetched parts of the surface was measured using AFM. Figure 11 shows the variation of the etch depth with time. A maximum effective etch rate of 2.2 nm/min was measured. Dissolution of the Au commences at a lower rate, where the nucleation of the etching occurs. Details on the nucleation mechanism of the Au etching will be published elsewhere.[44] Complete etching of the Au occurs after 25-30 mins, where the rate reduces to zero.

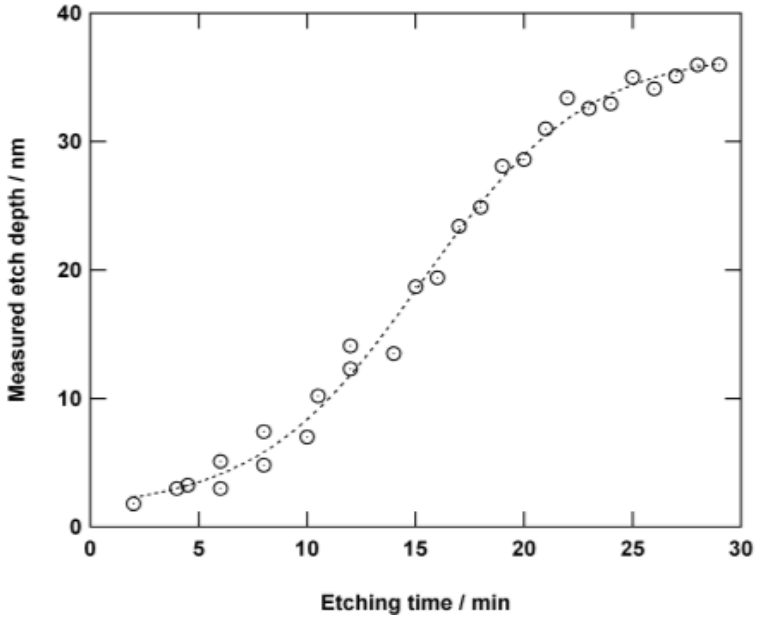


Figure 11. Variation of the measured etch depth with etching time. All samples were etched under identical conditions and the AFM depth measurements were performed immediately after the etching step. Half of each sample was covered with an inert resin which was removed with ethanol after etching.

In order to optimize this etching process and to explain why there are numerous reports of contrast and resolution problems for patterns etched using this resist-based technique in nanolithographic experiments, we observed the etching mechanism *in-situ* through the liquid without removal of the sample. In Fig. 12, the intensity of the 1st order maximum obtained by monitoring the diffracted laser light projected to a CCD as the exposed SAM surface was being etched is shown as a function of etching time. Again, the woven wire mesh was used as the exposure mask. As the bare regions of Au began to dissolve, the order heterogeneity of the mesh pattern being etched into the surface caused diffraction of the reflected light. As larger areas of the surface, sampled by the laser,

became heterogeneous due to the nucleation of the etching, the intensity of the diffraction pattern increased.

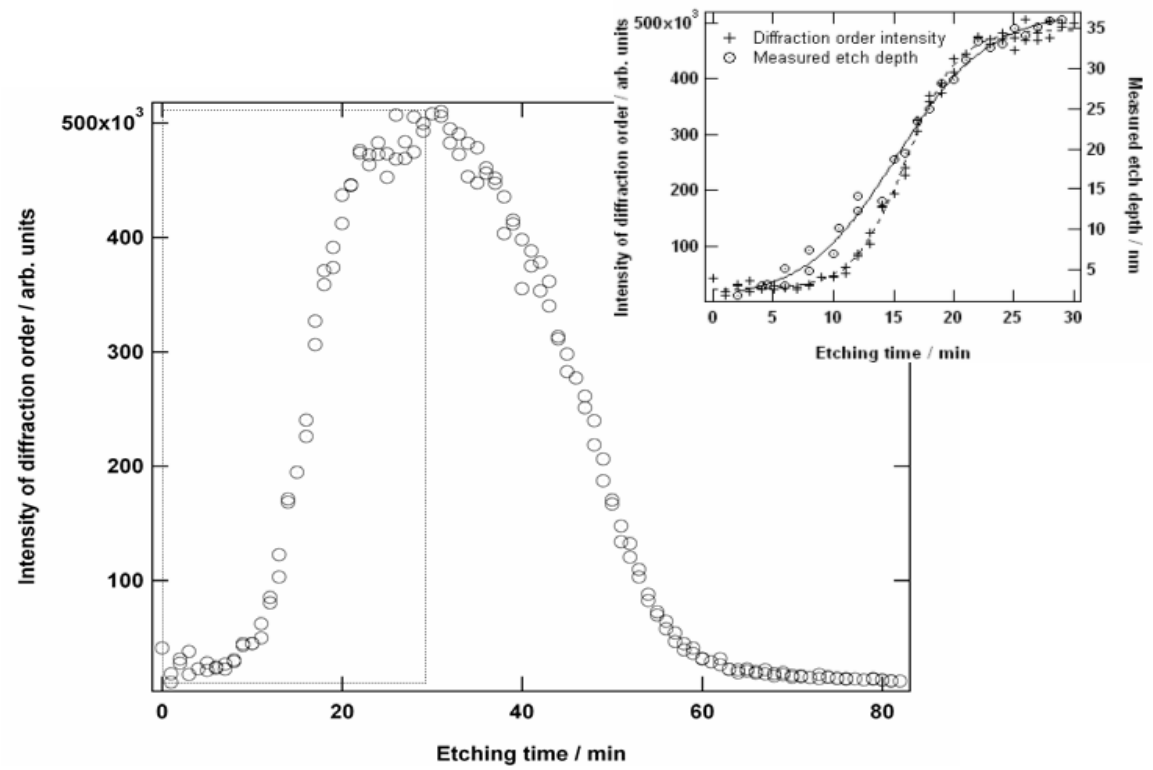


Figure 12. Variation of the first order diffraction spot intensity reflected from the Au surface with etching time. The intensity was measured using a calibrated CCD while the sample remained in the etching solution. A 5 mW He-Ne laser was used for incident radiation. *inset* Overlay of data from Figs. 10 and 11 showing the correlation between etch rate and measured *in-situ* diffraction intensity.

The intensity is a direct measure of the definition and density of the periodic structures on the surface, thus the measured intensity is proportional to the etch rate of the gold. Furthermore, the relative intensities of the diffraction orders remain unchanged as etching progresses, *i.e.* the 1st order always maintains highest intensity, then the second and so forth. Secondly, even though the relative intensities between successive orders do not vary, the intensity decreases with increasing order at a given time. This observation implies that the nucleation of the etching process is not random, *i.e.* etching begins to occur where the dose of Cs was the highest, at the position on the surface that was exposed to the center of the beam. Thus, the intensity of each order maxima is due to the nucleation of the etching process and not to the dissolution of the gold over areas that had already commenced etching. As observed in Fig. 12, the best pattern definition is observed after etching for 25-30 mins. This experiment thus illustrates the use of optical diffraction as a method to study the stochastic process of nucleation and corrosion. Also, by examination of higher order diffraction spots, it was possible to address the long range order of the nucleation process. The appearance of higher order diffraction spots that were not in succession was *not* observed indicating the nucleation does not occur randomly over the whole surface, but commences at a single point. In the inset to Fig. 12, the data from Fig. 11 is overlaid with the data from Fig. 12 and it can be observed that there is strong correlation between the diffraction intensity and the etch rate of the Au:1 surface. It is interesting to note that both curves have the same overall shape with the

maximum slope in both cases being at 50% of maximum. Furthermore, after 17 mins the data overlap, implying that the measured intensity is directly proportional to the amount of Au etched. A similar trend in diffraction intensity and dissolved thickness of bare gold was found by Kumar et al.[45]

Thus a minimum dose of 2 monolayers of Cs, or 2 Cs atoms per nonanethiol molecule, is necessary to expose the SAM. Studies of the etching of the exposed SAM indicate that an etching time of 25-30 mins allow for complete etching of the Au under exposed areas and the best feature definition. The studies show that for very small feature sizes that are in close proximity, merging of features can occur if the etching time is too long. As shown in Fig. 11, the diffraction intensity decreases indicating that the periodic pattern definition reduces. This observation implies that etching for over 30 mins results in the dissolution of the Au below unexposed SAM also.

CONCLUSIONS

The dependency of SAM coverage, subsequent post-etch pattern definition and minimum feature size on the quality of the Au substrate used in both physical mask and optical mask atomic nanolithographic experiments has been presented. In comparison, sputtered Au substrates yield much smoother surfaces and a higher density of {111} oriented grains than evaporated Au surfaces. Phase imaging with an atomic force microscope shows that the quality and percentage coverage of uniform alkanethiol monolayer adsorption was much greater for sputtered Au surfaces. Exposure of the monolayer with a laser-cooled Cs beam allowed determination of the minimum Cs dose (2 monolayers) to expose the SAM with lateral force microscopy. Suitable wet-etching in a cyanide based etchant, with etch rates of 2.2 nm min^{-1}, results in optimized pattern definition. These results are crucial in the advancement and optimization of processes for atomic nanolithography applications.

REFERENCES

(1) G. L. Timp, R. L. Behringer, D. M. Tennant, J. E. Cunningham, M. Prentiss, K. K. Berggren, *Phys. Rev. Lett.,* **69**, 1636 (1992)

(2) M. Prentiss, G. Timp, N. Bigelow, R. E. Behringer, J. E. Cunningham, *Appl. Phys. Lett.,* **60**, 1027 (1992)

(3) R. J. Celotta, R. Gupta, R.E. Scholten, J. J. McClelland, *J. Appl. Phys.*, **79**, 6079 (1996)

(4) H. Metcalf, P. van der Straten, *Phys. Rep.*, **244**, 203 (1994)

(5) C. S. Adams, M. Sigel, J. Mlynek, *Phys. Rep.*, **240**, 143 (1994)

(6) J. H. Thywissen, K. S. Johnson, R. Younkin, N. H. Dekker, K. K. Berggren, A. P. Chu, M. Prentiss, S. A. Lee, *J. Vac. Sci. Technol. B*, **15**, 2093 (1997)

(7) M. J. Lercel, H. G. Craighead, A. N. Parikh, K. Seshadri, D. L. Allara, *Appl. Phys. Lett.*, **68**, 1504 (1996)

(8) K. K. Berggren, A. Bard, J. L. Wilbur, J. D. Gillaspy, A. G. Helg, J. J. McClelland, S. L. Rolston, W. D. Phillips, M. Prentiss, G. M. Whitesides, *Science*, **269**, 1255 (1995)

(9) S. V. Atre, B. Lieberg, D. L. Allara, *Langmuir*, **11**, 3882 (1995) and references therein

(10) L. H. Dubois, R. G. Nuzzo, *Annu. Rev. Phys. Chem.*, **43**, 437 (1992)

(11) J. F. Ford, T. J. Vickers, C. K. Mann, J. B. Schlenoff, *Langmuir*, **12**, 1944 (1996)

(12) O. Chailapakul, L. Sun, C. Xu, R. M. Crooks, *J. Am. Chem. Soc.*, **115**, 12459

(1993)
(13) P. A. DiMilla, J. P. Folkers, H. A. Biebuyck, R. Haerter, G. P. Lopez, G. M. Whitesides, *J. Am. Chem. Soc.*, **116**, 2225 (1994)
(14) L. H. Dubois, B. R. Zegarski, R. G. Nuzzo, *J. Chem. Phys.*, **98**, 678 (1993)
(15) M. M. Walczak, C. A. Alves, B. D. Lamp, M. D. Porter, *J. Electroanal. Chem.*, **396**, 103 (1995)
(16) R. C. Tiberio, H. G. Craighead, M. Lercel, T. Lau, C. W. Sheen, D. L. Allara, *Appl. Phys. Lett.*, **62**, 476 (1993)
(17) L. Salem, *J. Chem. Phys.*, **37**, 2100 (1962)
(18) D. J. Lavrich, S. M. Wetterer, S. L. Bernasek, G. Scoles, *J. Phys. Chem.*, **102**, 3456 (1998)
(19) S. Sun, G. J. Leggett, *Nano Letters*, **2**, 1223 (2002)
(20) S. Sun, K. S. L. Chong, G. J. Leggett, *J. Am. Chem. Soc.*, **124**, 2414 (2002)
(21) Y. Xia, G. M. Whitesides, *Annu. Rev. Mater. Sci*., **28**, 153 (1998)
(22) Y. Xia, X. M. Zhao, G. M. Whitesides, *Micro. Eng.*, **32**, 255 (1996)
(23) J. L. Wilbur, A. Kumar, H. A. Biebuyck, E. Kim, G. M. Whitesides, *Nanotechnology*, **7**, 452 (1996)
(24) J. C. Love, D. B. Wolfe, M. L. Chabinyc, K. E. Paul, G. M. Whitesides, *J. Am. Chem. Soc.*, **124**, 1576 (2002)
(25) C. O'Dwyer, G. Gay, B. Viaris de Lesegno, J. Weiner, *Langmuir,* **21** (2004)
(26) M. T. Lee, C. C. Hsueh, M. S. Freund, G. S. Ferguson, *Langmuir*, **14**, 6419 (1998)
(27) B. D. Cullit, *Elements of X-ray Diffraction*, Addison-Wessely, Reading (1978)
(28) E. Delamarche, B. Michel, C. Gerber, D. Anselmetti, H.-J.Guntherodt, H. Wolf, H. Ringsdorf, *Langmuir* **10**, 2869 (1994)
(29) H. Berger, *Krist. Tech.*, **11**, 1171 (1976)
(30) G. E. Poirier, M. J. Tarlov, *Langmuir*, **10**, 2853 (1994)
(31) A. Camposeo, A. Piombini, F. Cervelli, F. Tantussi, F. Fuso, E. Arimondo, *Opt. Comm.*, **200**, 231 (2001)
(32) A. Camposeo, F. Cervelli, A. Piombini, F. Tantussi, F. Fuso, M. Allegrini, E. Arimondo, *Mat. Sci. Eng. C,* **23**, 217 (2003)
(33) J. Nogués, J. L. Costa, K. V. Rao, *Physica A*, **182**, 532 (1992)
(34) B. B. Mandelbrot, *The Fractal Geometry of Nature*, Freeman, San Francisco, (1982)
(35) B. B. Mandelbrot, D. E. Passoja, A. J. Paullay, *Nature,* **308**, 721 (1984)
(36) G. Reiss, H. Brückl, J. Vancea, R. Lecheeler, E. Hastreiter, *J. Appl. Phys.*, **70**, 523 (1991)
(37) T. Ohgi, H. Y. Sheng, Z. C. Dong, H. Nejoh, *Surf. Sci.*, **442**, 277 (1991)
(38) M. Kreis, F. Lison, D. Haubrich, D. Meschede, S. Nowak, T. Pfau, J. Mlynek, *Appl. Phys. B.*, **63**, 649 (1996)
(39) J. Li, K. S. Liang, N. Camillone III, T. Y. B. Leung, G. Scoles, *J. Chem. Phys.* **102**, 5012 (1995)
(40) A. M. Brittan, *Am. Sci.*, **62**, 402 (1974)
(41) F. A. Cotton, G. Wilkinson, *Advanced Inorganic Chemistry*, 4th ed., 966 Wiley, New York (1980)
(42) R. J. Puddephatt, *The Chemistry of Gold,* Elsevier, Amsterdam (1978)
(43) R. L. McCarley, Y. T. Kim, A. J. Bard, *J. Phys. Chem.*, **97**, 211 (1993)
(44) C. O'Dwyer, G. Gay, B. Viaris de Lesegno, J. Weiner, (unpublished)
(45) A. Kumar, H. A. Biebuyck, G. M. Whitesides, *Langmuir*, **10**, 1498 (1994)